Research Paper

GEOSPHERE

GEOSPHERE, v. 19, no. 5

https://doi.org/10.1130/GES02633.1

7 figures; 3 tables

CORRESPONDENCE: e.salomon@outlook.de

CITATION: Salomon, E., 2023, Rate of E–W extension in the Volcanic Tableland, California (USA): A comparison of strain rates on two different timescales: Geosphere, v. 19, no. 5, p. 1280–1290, https://doi.org/10.1130/GES02633.1.

Science Editor: David E. Fastovsky
Associate Editor: Michael L. Williams

Received 19 December 2022
Revision received 24 April 2023
Accepted 15 June 2023

Published online 10 August 2023

Rate of E–W extension in the Volcanic Tableland, California (USA): A comparison of strain rates on two different timescales

Eric Salomon

Friedrich-Alexander-Universität Erlangen-Nürnberg, GeoZentrum Nordbayern, Schlossgarten 5, 91054 Erlangen, Germany

ABSTRACT

The Eastern California shear zone (USA) is a broad zone of transtensional deformation related to the relative motion between the Pacific and North American plates. Due to its active deformation and seismicity, the zone receives great attention, with specific focus on slip rates of major active faults. To contribute to a better understanding of the long-term strain accumulation in this zone, this study quantifies the long-term E–W-directed extensional strain rate based on the analysis of N–S-trending normal fault scarps in the 765-k.y.-old Bishop tuff (Volcanic Tableland). The average extensional strain rate determined over the past 765 k.y. is 0.29 ± 0.10 mm/yr per 10 km (29 ± 10 nanostrain/yr) and similar to the current rate of elastic strain accumulation rate in the Volcanic Tableland (0.30 ± 0.13 mm/yr per 10 km; 30 ± 13 nanostrain/yr) determined by Global Positioning System (GPS) data. The present-day E–W strain rate across the entire Eastern California shear zone at the latitude of the Volcanic Tableland is 0.36 ± 0.05 mm/yr per 10 km (36 ± 5 nanostrain/yr). This suggests that the local rate of E–W extension has not changed significantly since the mid-Pleistocene. Furthermore, if the Volcanic Tableland is representative of the greater region, as the GPS data suggest, this would also indicate a constant extension rate across the Eastern California shear zone at the latitude of ~37.5°N over the 765 k.y. time period. These results suggest that late Pleistocene and Holocene extension rates of major faults in this zone can be interpreted in light of a presumably unchanged far-field stress system since at least the mid-Pleistocene.

INTRODUCTION

Strain rates of fault zones are known to vary through time (e.g., Wallace, 1987; Sieh et al., 2008; Nicol et al., 2009; Cowie et al., 2012; Mechernich et al., 2018). To better understand the implications of short-term rates, it is therefore important to have knowledge of longer-term deformation rates as a reference point. Consequently, studies comparing deformation rates based on geodetic and geologic data across different timescales around the globe are numerous (e.g., Kreemer et al., 2004; Papanikolaou et al., 2005; Nicol and Wallace, 2007; Cowgill et al., 2009; Faure Walker et al., 2010; Mazzotti et al., 2011; Karakhanyan et al., 2013; Salomon et al., 2013; Hetzel et al., 2019; Iezzi et al., 2021). An important aspect is the timeframe used to interpret the respective rate. Rates determined by geodetic methods, e.g., the Global Positioning System (GPS), commonly reflect a period of <30 years and may therefore record any phase of a seismic cycle (e.g., Thatcher, 1983; Meade et al., 2013). Rates covering the Holocene or late Pleistocene may capture a period of earthquake clustering or quiescence (e.g., Nicol et al., 2009; Salditch et al., 2020; Martín-Banda et al., 2021). Intermediate-term (~300 k.y.–1 m.y.) rates are more likely to represent the true present tectonic (or interseismic) rate, while rates concerning >~1 m.y. may already be affected by changes in plate motion (e.g., Friedrich et al., 2003; Mouslopoulou et al., 2009).

A region whose deformation history has received considerable attention is the Eastern California shear zone/Walker Lane belt (see inset map of Fig. 1 for location) along the western boundary of the Basin and Range Province, USA (e.g., Reheis and Dixon, 1996; Berry, 1997; Lee et al., 2001, 2009; Unruh et al., 2003; Kirby et al., 2006, 2008; Guest et al., 2007; Le et al., 2007; Oskin et al., 2007, 2008; Ganev et al., 2010; Pérouse and Wernicke, 2017; DeLano et al., 2019; Lifton et al., 2021). Second to the San Andreas fault system, this zone accommodates ~25% of the strain related to dextral transtensional motion of the Pacific plate relative to the North American plate (e.g., Dokka and Travis, 1990; Dixon et al., 2000; Miller et al., 2001) and is subject to a high degree of seismicity (Hauksson, 2000). Of specific interest is the Owens Valley, one of the key areas in the Eastern California shear zone, which was hit by a M_w 7.4–7.9 earthquake in 1872 that was one of the largest historical earthquakes in the USA (Beanland and Clark, 1994; Hough and Hutton, 2008).

To improve our understanding of ongoing deformation in the Owens Valley and the Eastern California shear zone, this study compares GPS data with geologic data that record extensional strain since the mid-Pleistocene. A key element of the analysis is the ~765-k.y.-old Bishop tuff on the Volcanic Tableland (Sarna-Wojcicki et al., 2000; Andersen et al., 2017), which has experienced only ~1–2 m of erosion (Goethals et al., 2009; Fig. 1) and is dissected by a population of normal faults (Bateman et al., 1965; Sheridan, 1970; Dawers et al., 1993; Pinter, 1995; Fig. 2). Therefore, the Bishop tuff serves as a perfect time-marker for determining long-term permanent deformation. In addition, a number of GPS stations distributed in the area have recorded ground motions for ~15 years and provide an excellent database for assessing the present-day rate of elastic strain accumulation (Blewitt et al., 2018). This comparison provides a long-term reference to aid in the interpretation of

Eric Salomon https://orcid.org/0000-0003-1297-4972

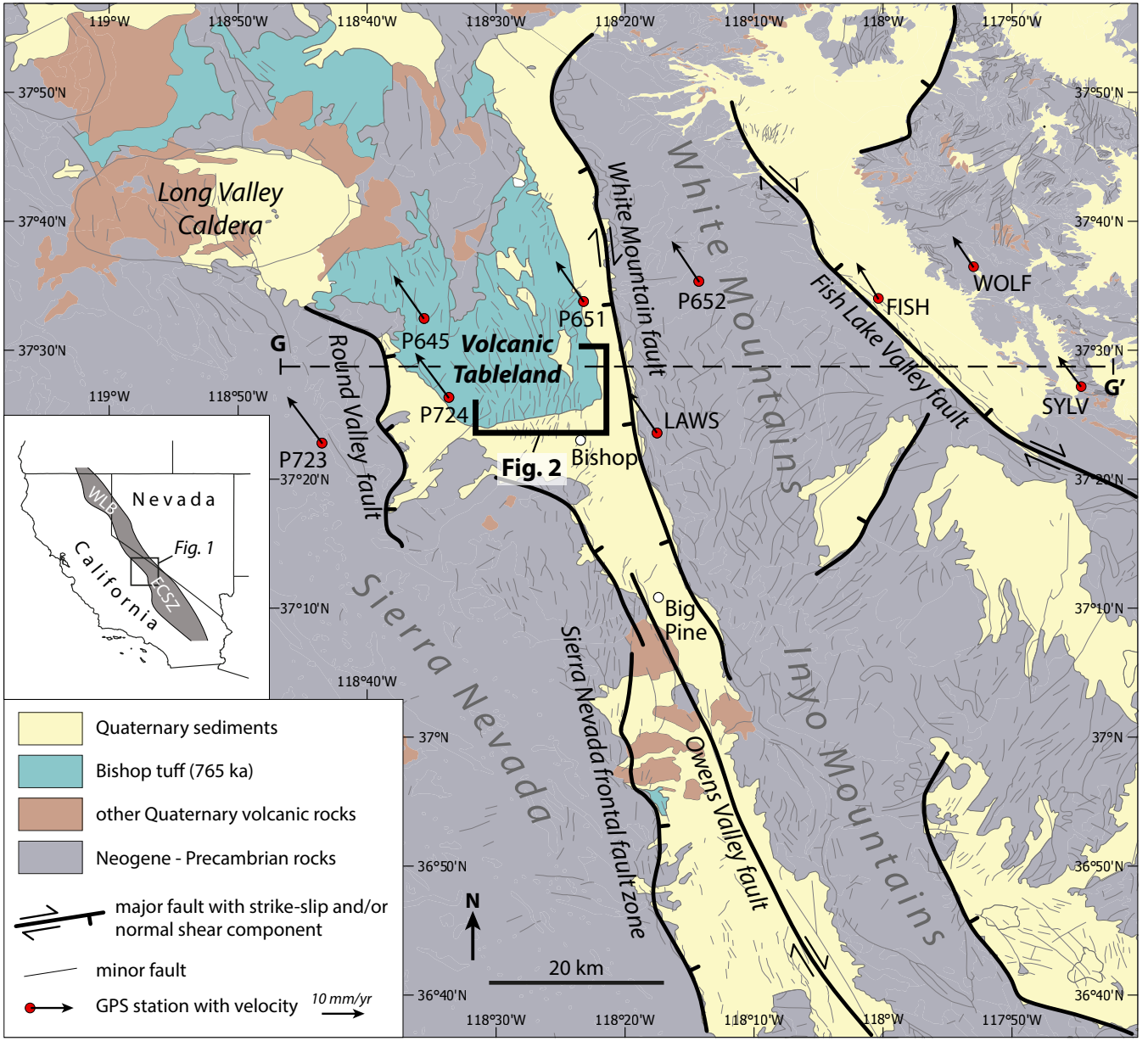

Figure 1. Simplified geological map overview of the study region (modified after the State Geologic Map Compilation; Horton, 2017). GPS stations and data used in this study are from Kreemer and Young (2022; cf. Table 2). Major faults are after Lee et al. (2009). Extent of Walker Lane belt (WLB) and Eastern California shear zone (ECSZ) in the inset map are after Pérouse and Wernicke (2017).

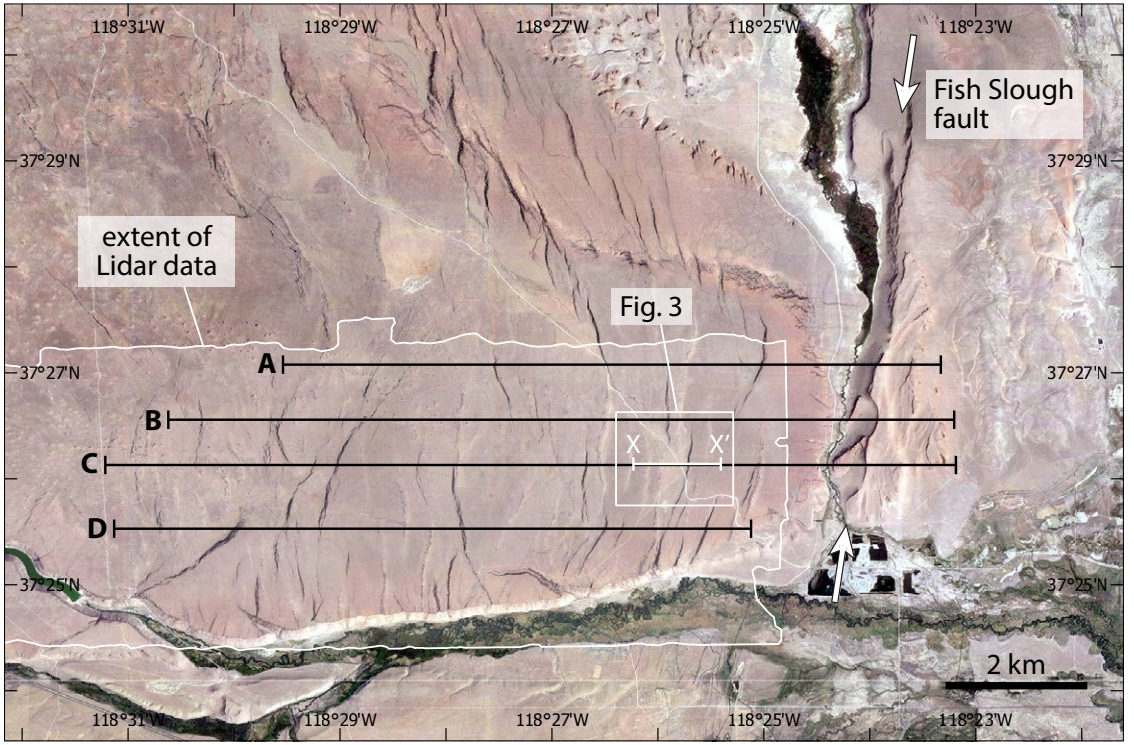

Figure 2. Satellite image of study area with locations of the four E–W profiles across the Volcanic Tableland whose surface is formed by the 765-k.y.-old Bishop tuff. Normal faults cutting through the Bishop tuff form well-preserved fault scarps. In the image, west-dipping fault scarps appear with shadows due to westward-directed sunlight. The west-dipping Fish Slough fault, indicated by white arrows, is the largest normal fault in the study area. Image is from Google Earth.

late Pleistocene or younger fault slip rates in the Eastern California shear zone.

GEOLOGIC SETTING

The ~15-km-wide Volcanic Tableland is located in the northern section of the ~120-km-long, NNW-trending Owens Valley, which separates the Sierra Nevada block in the west from the White/Inyo Mountains block in the east (Fig. 1). The Owens Valley is part of the ~100-km-wide Eastern California shear zone, which accommodates long-lived extension and dextral strike-slip in response to initially westward and then northwestward motion of the Sierra Nevada block with respect to stable North America. The Eastern California shear zone formed in the middle Miocene and experienced ~E–W-directed extension until the early Pliocene, while dextral transtension has dominated since the late Pliocene (e.g., Stockli et al., 2003; Lee et al., 2009; Stevens et al., 2013, and references therein). Presently, this zone accommodates ~25% of the dextral strike-slip motion between the Pacific and North American plates (e.g., Dixon et al., 2000; Miller et al., 2001) and is subject to a transtensional rate of 10.6 ± 0.5 mm/yr toward N37°W (Lifton et al., 2013).

The northern Owens Valley is bounded to the east by the White Mountains fault (Fig. 1), whose age of initiation is considered to be either ca. 12 Ma (Stockli et al., 2003) or ca. 3 Ma (Lueddecke et al., 1998). In any case, significant extension and dextral strike-slip faulting occurred on this fault after ca. 3 Ma. To the west, at the latitude of the Volcanic Tableland, the northern Owens Valley is bounded by the Round Valley fault, whose age of initiation is unclear. This fault is generally described as a normal fault (dePolo et al., 1993), although a dextral component also exists (Phillips and Majkowski, 2011).

The Volcanic Tableland is formed by the Bishop tuff, which erupted from the Long Valley Caldera (Fig. 1) and is dated to 758.9 ± 1.8 ka (1σ; Sarna-Wojcicki et al., 2000) and 764.8 ± 0.3 ka (2σ; Andersen et al., 2017). The surface of the Bishop tuff is remarkably well preserved. High cosmogenic-nuclide concentrations in the tuff indicate that it has experienced no more than ~1–2 m of erosion since its deposition (Goethals et al., 2009). A population of ~N–S-trending normal faults has since formed and dissects the Bishop tuff as shown by well-developed fault scarps on the Volcanic Tableland (e.g., Bateman et al., 1965; Sheridan, 1970; Dawers et al., 1993; Pinter, 1995). Normal faulting

on the Volcanic Tableland has been continuously active through the Pleistocene, as indicated by offset fluvial terraces at its southern margin (Ferrill et al., 2016), and it is still active today (Lienkaemper et al., 1987).

METHODOLOGY

Strain Rate Derived from Fault Scarp Analysis

The ~N–S-trending normal faults cutting through the Bishop tuff indicate approximate E–W extension (Pinter, 1995; Ferrill et al., 1999; McGinnis et al., 2009). To determine the E–W-directed extension from these faults, the vertical offsets of each fault along four E–W profiles across the Volcanic Tableland were measured (Figs. 2–4). Faults crossed by the profiles were identified by analyzing data from a Lidar-based digital elevation model (DEM) collected by the National Center for Airborne Laser Mapping (2016: resolution of ~0.3 m in the horizontal plane), the Google Earth elevation model (<10 m resolution in the horizontal plane), Google Earth satellite imagery (0.2 m resolution), hillshade models, and published geological maps (Dawers et al., 1993; Pinter, 1995; Ferrill et al., 2016). Vertical offsets were determined using the Lidar-based DEM. For profile sections outside of the Lidar mapping area (Fig. 2), the Google Earth elevation model was used, which covers the Fish Slough fault zone along profiles A–C (Fig. 2). The vertical offset of a normal fault was measured as the vertical difference between the interpolated hanging and footwall surface at the midpoint of the fault scarp's cross-profile (Figs. 3 and 4; cf. Bucknam and Anderson, 1979). Interpolating the flat surfaces of the hanging and footwall toward the fault allows the offset measurement to be unaffected by scarp erosion and near-scarp deposition that occurs on the Volcanic Tableland (Pinter, 1995) and is responsible for rounding the scarp profile.

For the sections covered by Lidar data, surface interpolation was performed by linear regression to fit a line through the data points. These surfaces consistently have a standard deviation of <0.3 m. Therefore, an uncertainty of ±0.6 m was added to each vertical offset measurement. A different approach was required for the Fish Slough fault zone located outside of the Lidar data, as only elevation profile graphs can be analyzed. Here, I visually fitted a range of admissible interpolation lines of different dips through the hanging wall and footwall surfaces. The vertical offset therefore varies with the dips of these lines. I used the mean between the smallest and largest offset obtained and the difference to the smallest/largest offset measured as the uncertainty.

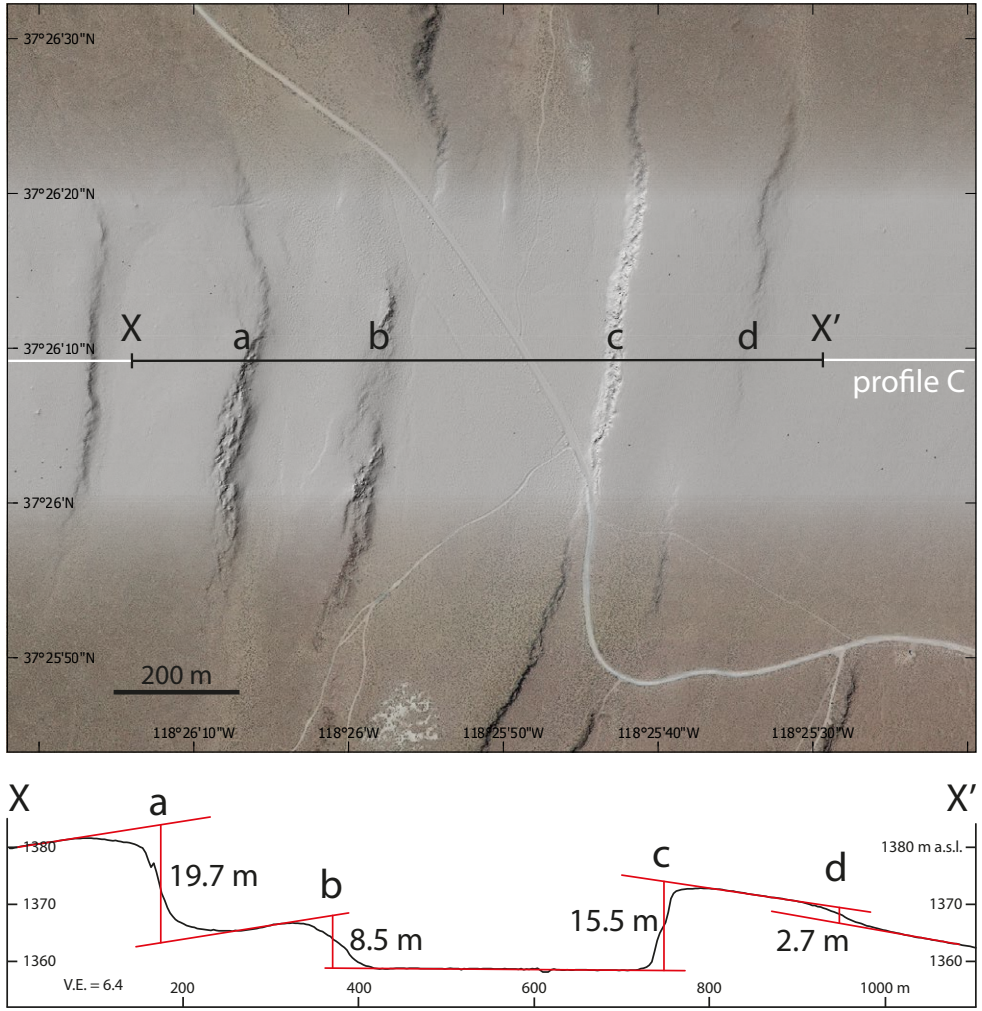

Figure 3. Subsection of profile C (see Fig. 2 for location) illustrates the high quality of the elevation model based on Lidar data (National Center for Airborne Laser Mapping, 2016) and satellite imagery (Google Earth). Vertical offsets determined at each fault scarp are the vertical distance between the two red interpolation lines in the fault footwall and the hanging wall. V.E.—vertical exaggeration.

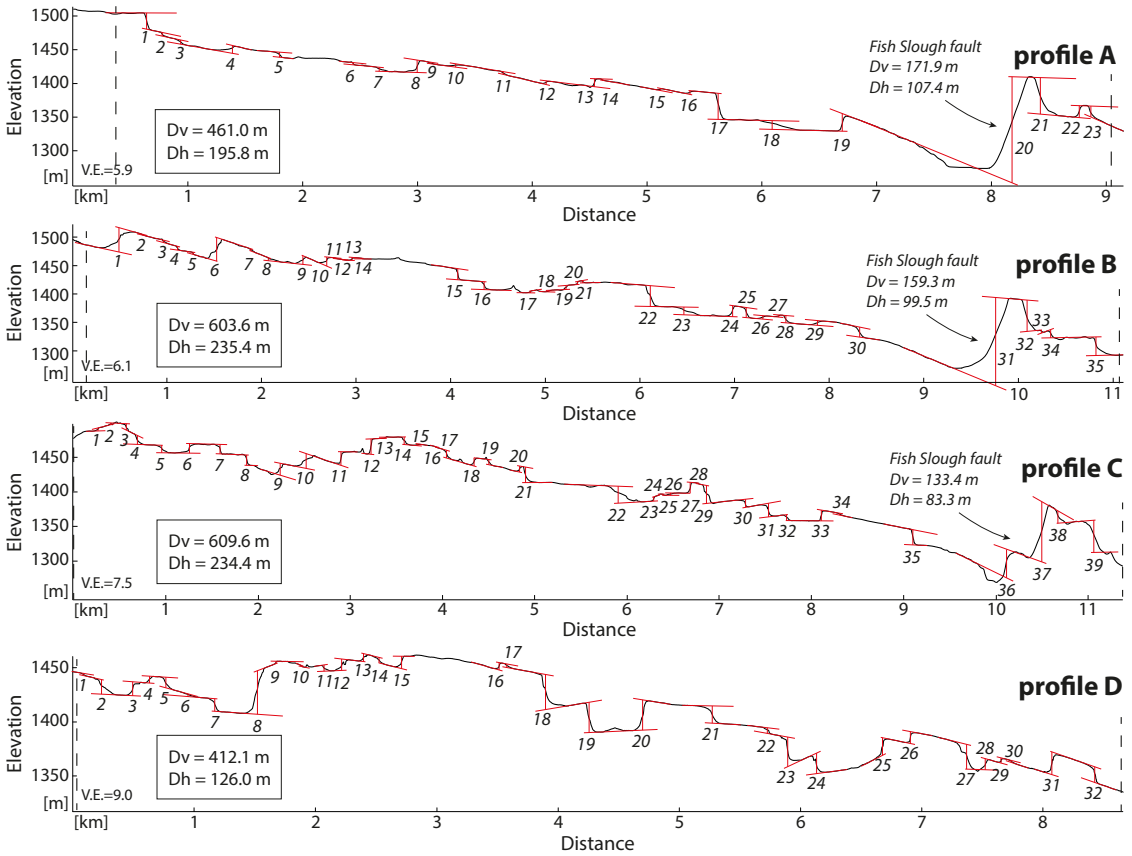

Figure 4. E–W profiles across the Volcanic Tableland (see Fig. 2 for position of profiles). Vertical displacement determined at each fault scarp is the vertical distance between the red lines. Numbers refer to the individual faults (see Table A1). Two vertical dashed lines on each profile indicate the profile length used for the strain rate calculation. Dv—total vertical displacement along profile; Dh—total horizontal displacement along profile; V.E.—vertical exaggeration. Displacements for each fault are given in Table A1.

Horizontal extension was calculated using this vertical offset and an assumed fault dip angle. From the southern margin of the Volcanic Tableland, McGinnis et al. (2009) reported dip values of 63 faults that range between 41° and 88°, with an average of 73°. For the calculation of the horizontal extension, I relied on these data, which are available from a stereographic projection plot (fig. 3B of McGinnis et al., 2009). The data were extracted from this plot using Stereonet software (Allmendinger et al., 2012; Cardozo and Allmendinger, 2013), and the resulting values are consistent with those reported by McGinnis et al. (2009), with a minimum of 41°, a maximum of 88°, an average of 72.2°, and a median of 73° (Fig. 5). As the data show a skewed distribution, I used the median for the horizontal extension calculation and the first and third quartiles (64° and 81°; Fig. 5) as a ± 9° uncertainty envelope (Table 1). A different fault dip was used for the Fish Slough fault, the largest fault on the Volcanic Tableland (Fig. 2), for which Phillips and Majkowski (2011) determined a dip angle of 58°. Here, I used a dip value of 58 ± 9° for this specific fault. Along each of the four E–W profiles, the total horizontal displacement is the sum of each fault's horizontal offset crossed by the respective profile. The uncertainties of horizontal displacements were calculated with the Gaussian uncertainty propagation (Table A1).

The extension rate along each profile was calculated as the total horizontal displacement along the respective profile divided by the age of the Bishop tuff. Here, the 765 ka age of Andersen et al. (2017) was used; the small uncertainty of ± 0.3 ka (2σ) was neglected in the calculation. The strain rate was then calculated by dividing the extension rate by the original length of the profile. The original length of the profile is the present-day length minus the total horizontal displacement along the profile. For a better visualization, the strain rate is given as mm/yr per 10 km as well as in nanostrain/yr (Table 1).

With the Lidar-derived DEM, hillshade models, and visual inspection of Google Earth optical satellite imagery, fault scarps with >0.75 m of vertical offset were detected in this study (Table A1). The Google Earth DEM resolution that was used for

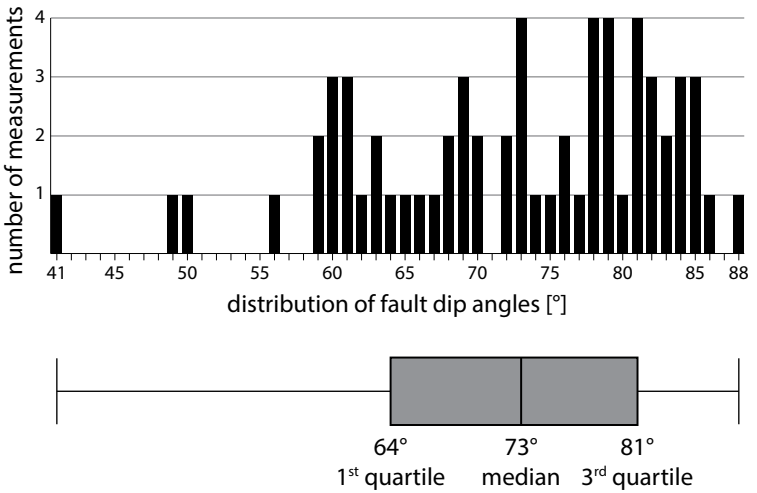

Figure 5. Histogram and box-and-whisker plot of fault dip data from the Volcanic Tableland (collected by McGinnis et al., 2009; cf. fig. 3B of McGinnis et al., 2009). The 73° median of the fault population is used in the present study as the fault dip angle, with the first and third quartiles as uncertainty envelopes (64–81°).

profile sections not covered by the Lidar data is poorer. These sections concern the Fish Slough fault zone (Fig. 2). Nevertheless, judging from the assessment of the satellite imagery, the significant major faults were captured by the Google Earth DEM. Fault scarps with offsets of <0.75 m, which were not detected, resulted in a slight underestimation of the total vertical offset and, thus, the amount of extension. This is a common problem in stretching estimates based on fault populations (Fossen, 2020) and can be addressed by using a power-law distribution of offset fault populations (Walsh et al., 1991; Marrett and Allmendinger, 1992; Gauthier and Lake, 1993). If fault throw is plotted against the cumulative number of fault measurements in log-log space (Fig. 6), the power-law relation can be expressed as $N = a\,S^{-D}$, where N is the cumulative number of fault measurement, a is a constant, S is the vertical fault throw, and D is the slope of the regression line of the population (Marrett and Allmendinger, 1992; Walsh et al., 1991). Although this power-law relationship is rarely perfect, it appears to be valid for segments of the fault throw populations (Fossen and Rørnes, 1996). Here, the flat segment below throw values of <10 m was used to calculate slope D (Fig. 6). Using the equation above, it is possible to calculate the number of faults with offsets of between 0.75 m and 0.01 m that remained undetected and estimate their cumulative vertical throw. For profile A, this throw is 8.7 m; for profile B, 4.0 m; for profile C, 6.4 m; and for profile D, 5.7 m. These values were added to the vertical throw determined for each of the four profiles, A–D.

TABLE 1. STRAIN RATES DERIVED FROM FAULT SCARP ANALYSIS IN BISHOP TUFF ON VOLCANIC TABLELAND

Profile	Profile length (present day, in km)	Total vertical fault offset along profile (m)*,**	Horizontal extension (m) with fault dip angle of 73 ± 9°***	Horizontal extension (m) per 10 km	Extension rate per 10 km (mm/yr)	Strain rate (nstr/yr)
A	8.70	469.7 ± 34.4	198.5 ± 63.1	228.2 ± 72.5	0.31 ± 0.10	31 ± 10
B	10.90	607.4 ± 15.0	236.6 ± 84.0	217.1 ± 77.1	0.29 ± 0.10	29 ± 10
C	11.40	616.1 ± 20.7	236.4 ± 87.0	207.4 ± 76.3	0.28 ± 0.10	28 ± 10
D	8.60	417.8 ± 6.8	127.7 ± 70.8	148.5 ± 82.3	0.20 ± 0.11	20 ± 11

*For individual fault offsets, see Table A1 in Appendix section.
**Includes calculated vertical offset from faults below detection limit (8.7 m for A, 4.0 m for B, 6.4 m for C, 5.7 m for D).
***Fish Slough fault assigned with 58 ± 9° dip angle.

Strain Rate Derived from GPS Data

In the study area, a network of GPS stations exists, with recordings since 2005. The data are available from the Nevada Geodetic Lab (Blewitt et al., 2018; http://geodesy.unr.edu/). In addition, Kreemer and Young (2022) corrected the GPS velocities recorded by this network for postseismic viscoelastic relaxation, which is the response of the viscoelastic layers of the lithosphere to an earthquake and can impact the Earth's surface motions for decades after an earthquake (e.g., Reilinger, 1986; Hetland and Hager, 2005; Hampel and Hetzel, 2015). A correction for this effect therefore provides a more reliable picture of the interseismic strain rate.

Across the Eastern California shear zone, nine GPS stations exist at the approximate latitude of the Volcanic Tableland, with data from both Blewitt et al. (2018) and Kreemer and Young (2022). These data are considered here (Fig. 1; Table 2). By plotting the east-directed velocities of these stations relative to stable North America onto an E–W profile, I determined the present-day E–W strain rate. The strain rate was calculated by least-square regression (Fig. 7; cf. Xu et al., 2021).

RESULTS

The analysis of fault scarps on the Volcanic Tableland across the four E–W profiles yields a large range of vertical offsets from 0.8 m to 57.2 m (excluding the Fish Slough fault), which converts to horizontal displacements of between 0.2 m and 17.5 m (with a fault dip of 73°; Table A1). For the Fish Slough fault (dip angle of 58°), the vertical offset ranges between

TABLE 2. GPS VELOCITIES RECORDED AT STATIONS LOCATED NEAR THE APPROXIMATE LATITUDE OF THE VOLCANIC TABLELAND

GPS Station	Longitude (°E)	Latitude (°N)	Recording since	Fom Blewitt et al. (2018)* (mm/yr)		From Kreemer and Young (2022)* (mm/yr)	
				vE** ± 3σ	vN** ± 3σ	vE ± 1σ	vN ± 1σ
P645	118.593	37.541	2008	–6.21 ± 0.22	8.18 ± 0.19	–7.05 ± 0.18	10.08 ± 0.16
P651	118.387	37.563	2006	–5.56 ± 0.17	7.35 ± 0.16	–6.50 ± 0.15	9.47 ± 0.14
P652	118.238	37.589	2007	–5.26 ± 0.20	6.60 ± 0.18	–6.39 ± 0.17	9.52 ± 0.15
P723	118.725	37.380	2007	–7.71 ± 0.29	9.13 ± 0.25	–8.18 ± 0.28	10.88 ± 0.21
P724	118.561	37.439	2008	–7.10 ± 0.22	8.56 ± 0.18	–7.83 ± 0.19	10.50 ± 0.16
LAWS	118.292	37.393	2006	–5.78 ± 0.36	7.34 ± 0.33	–6.69 ± 0.11	9.66 ± 0.11
FISH	118.006	37.567	2005	–4.23 ± 0.51	5.59 ± 0.33	–5.13 ± 0.13	8.49 ± 0.11
WOLF	117.883	37.608	2005	–4.21 ± 0.34	4.70 ± 0.29	–4.88 ± 0.19	7.27 ± 0.10
SYLV	117.744	37.453	2005	–4.58 ± 0.25	4.43 ± 0.26	–5.38 ± 0.12	7.12 ± 0.13

Notes: Also see Figure 1 for location.
*Note that velocities from Blewitt et al. (2018) are provided with 3σ uncertainty and velocities from Kreemer and Young with 1σ.
**vE and vN are east- and north-directed velocity components, respectively, of the GPS station.

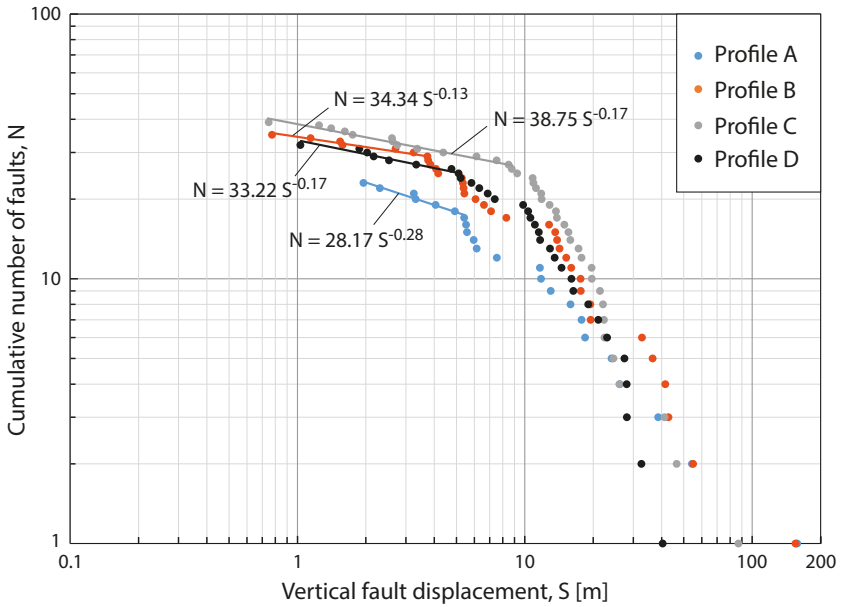

Figure 6. Log-log plot of vertical fault displacement (S) versus cumulative number of faults (N) measured along each profile (cf. Fig. 4; Table A1) used for the assessment of displacement accommodated by faults smaller than the detection limit of 0.75 m. The power-law relationship allows calculation of the number of these faults in the range of 0.1–0.75 m (see Methodology section for further explanation).

133.4 m and 171.9 m, which translates to a horizontal extension of 83.3–107.4 m (Fig. 4; Table A1). The total horizontal extension along profiles A–D ranges from 128 m to 237 m (Table 1). Keeping in mind the different lengths of the four profiles, formulating these values as per 10 km provides a better comparison. Accordingly, the range of horizontal extension is 149–228 m per 10 km (Table 1). Taking into account the age of the Bishop tuff (765 ka), the extensional strain rates are between 0.20 ± 0.11 mm/yr and 0.31 ± 0.10 mm/yr per 10 km (Table 1).

The E–W-directed extensional strain rate derived from the GPS velocities of Blewitt et al. (2018) is 0.38 ± 0.06 mm/yr per 10 km (Fig. 7A). Using the GPS velocities corrected for postseismic relaxation (Kreemer and Young, 2022) yields a slightly lower strain rate of 0.36 ± 0.05 mm/yr per 10 km (Fig. 7B). In the following sections, the latter rate is used, because it is considered to be a more realistic representation of the present-day interseismic E–W strain rate due to the correction for postseismic relaxation.

DISCUSSION

The E–W strain rates that were determined from the measurements of fault offsets along profiles A–C across the mid-Pleistocene Bishop tuff are very similar to one another, with average values of 0.31, 0.29, and 0.28 mm/yr per 10 km (Table 1). Despite an overlap of uncertainties of the strain rates, the lower strain rate of 0.20 mm/yr per 10 km of profile D diverges notably from those of the other three profiles. This profile is the only one that does not extend across the Fish Slough fault, because this fault is eroded at the latitude of the profile (Fig. 2). The effect of the Fish Slough fault on the strain rate can be explored by extending profile D to the east beyond the trace of the fault (to a total length of 11.2 km) and adding the horizontal displacement of the Fish Slough fault and adjacent eastward-facing faults of profile C (106.4 m). This approach leads to a strain rate of 0.28 mm/yr per 10 km for profile D—a value similar to those of profiles A–C. This highlights that the distribution of strain across the Volcanic Tableland is not uniform and that the Fish Slough fault contributes significantly to the

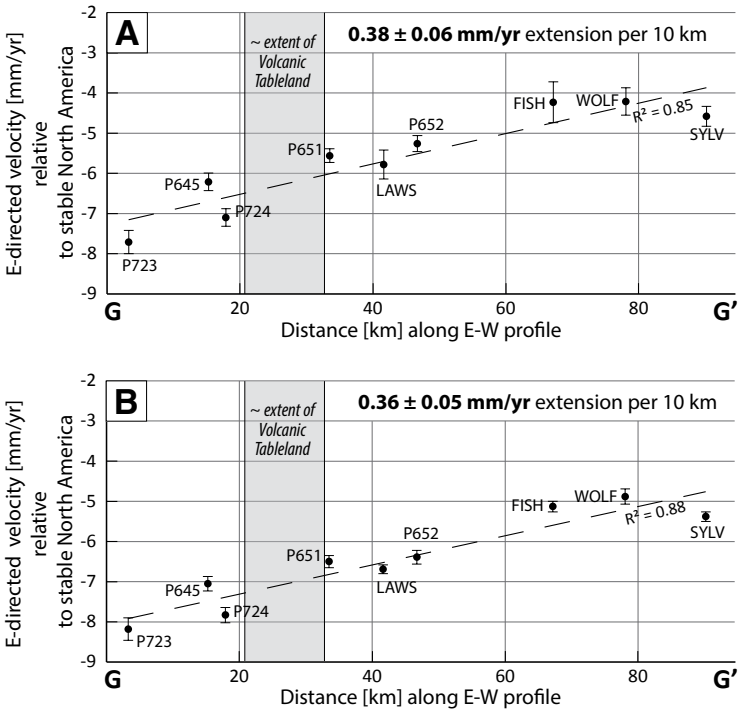

Figure 7. Plots showing the E-directed velocity components of GPS stations at the latitude of the Volcanic Tableland along an E–W profile across the Volcanic Tableland and the Eastern California shear zone (for location, see Fig. 1). (A) GPS velocities of Blewitt et al. (2018), and (B) GPS velocities of Kreemer and Young (2022), which are corrected for postseismic relaxation (cf. Table 2). GPS velocities indicate E–W extension at a rate of 0.38 ± 0.06 mm/yr in panel A, and 0.36 ± 0.05 mm/yr per 10 km in panel B.

accumulation of permanent strain. In summary, the E–W strain rates obtained for profiles A–C, with an average of 0.29 ± 0.10 mm/yr per 10 km, are interpreted as reliable.

A similar approach of determining extension across the Volcanic Tableland was conducted by Pinter (1995), who measured vertical fault offsets in the field along a single 14-km-long E–W profile with the pace-and-Brunton handheld compass approach and assumed an average fault dip of 60° to calculate the amount of extension. Pinter (1995) reported a total vertical displacement of 500 m. For a dip angle of 73 ± 9°, as used in the present study, this value yields a strain rate of 0.14 ± 0.08 mm/yr per 10 km, which is significantly lower than the rates obtained for profiles A–C. As the offsets obtained from the individual scarps were not provided by Pinter (1995), assessment of the data and the result is difficult. The discrepancy may be due to the fact that the profile of Pinter (1995) does not cover the Fish Slough fault, which has a significant impact on the strain rate in the Volcanic Tableland as discussed above.

GPS data indicate an E–W extensional strain rate of 0.36 ± 0.05 mm/yr per 10 km across the Eastern California shear zone over the past ~15 years, if the GPS velocities corrected for viscoelastic relaxation are used (Kreemer and Young, 2022). This rate reflects the accumulation of elastic strain that is currently induced to the Eastern California shear zone by the far-field tectonic stress. This regional extension rate can be compared with a local extension rate of the Volcanic Tableland. When using the two GPS stations P645 and P651 (Figs. 1 and 7), which lie at approximately the same latitude and directly east and west of the Volcanic Tableland, their W-directed velocity components yield an extensional strain rate of 0.30 ± 0.13 mm/yr per 10 km. The similarity between this local rate and the more regional rate shows that the Volcanic Tableland is currently accumulating elastic strain at the same rate as the Eastern California shear zone at the latitude of ~37.5°N.

Both the local and the regional present-day extension rates derived from GPS data are similar to the one obtained from the fault-scarp analysis of the Volcanic Tableland (i.e., ~0.29 mm/yr per 10 km). This finding indicates that the Volcanic Tableland is currently experiencing extension at a similar rate as the timed-average rate over the last 765 k.y. If the same applies to the entire Eastern California shear zone, this would imply that the E–W-directed strain rate induced by the far-field stress system has, on average, remained the same since the mid-Pleistocene. Of course, it cannot be ruled out that the rate has varied over time during this period, and a phase that is similar to that of the 765 k.y. average may now be underway. Assuming that the current strain rate across the Eastern California shear zone equals the long-term time-averaged rate allows calculation of the total amount of extension over the past 765 k.y., an extensional strain rate of 0.36 ± 0.05 mm/yr per 10 km and using 87 km as the extent of the Eastern California shear zone (i.e., the distance between GPS stations P723 – SYLV; Fig. 1) yields a total E–W extension of 2.4 ± 0.3 km.

CONCLUSIONS

The analysis of normal fault scarps in the mid-Pleistocene Bishop tuff reveals an E–W strain rate over the past 765 k.y. that is similar to the present-day strain rate derived from geodetic measurements in the Volcanic Tableland and across the entire Eastern California shear zone at this latitude. This finding suggests that the accumulation of permanent strain by normal faulting has remained constant since the

eruption of the Bishop tuff and the formation of the Volcanic Tableland. If the Volcanic Tableland is representative of the greater region (as GPS data suggest), this would also indicate a constant extension rate across the Eastern California shear zone over this time period. These results underpin that extension rates assessed in the Eastern California shear zone at younger, shorter timescales should be interpreted in the context of a constant extensional strain accumulation since the mid-Pleistocene.

ACKNOWLEDGMENTS

Ralf Hetzel and Silke Mechernich are thanked for helpful and constructive discussions on the subject. Constructive comments by two anonymous reviewers are gratefully acknowledged. David E. Fastovsky and Michael L. Williams are thanked for editorial handling. Salomon acknowledges financial support by Deutsche Forschungsgemeinschaft and Friedrich-Alexander-Universität Erlangen-Nürnberg within the funding program Open Access Publication Funding.

APPENDIX

TABLE A1. VALUES OF VERTICAL OFFSET AND HORIZONTAL EXTENSION FOR ALL FAULT SCARPS ALONG THE FOUR E–W PROFILES ON THE VOLCANIC TABLELAND

PROFILE A			PROFILE B			PROFILE C			PROFILE D		
Fault ID	Vertical offset (m)	Horizontal displacement (m)	Fault ID	Vertical offset (m)	Horizontal displacement (m)	Fault ID	Vertical offset (m)	Horizontal displacement (m)	Fault ID	Vertical offset (m)	Horizontal displacement (m)
1	24.0 ± 0.6	7.3 ± 2.0*	1	42.8 ± 0.6	13.1 ± 2.7	1	4.4 ± 0.6	1.3 ± 0.9	1	2.0 ± 0.6	0.6 ± 0.6
2	5.4 ± 0.6	1.7 ± 1.0	2	1.6 ± 0.6	0.5 ± 0.6	2	2.6 ± 0.6	0.8 ± 0.7	2	13.5 ± 0.6	4.1 ± 1.5
3	6.1 ± 0.6	1.9 ± 1.0	3	4.2 ± 0.6	1.3 ± 0.9	3	9.2 ± 0.6	2.8 ± 1.3	3	12.9 ± 0.6	3.9 ± 1.5
4	11.6 ± 0.6	3.6 ± 1.4	4	6.6 ± 0.6	2.0 ± 1.1	4	12.9 ± 0.6	3.9 ± 1.5	4	6.3 ± 0.6	1.9 ± 1.1
5	7.5 ± 0.6	2.3 ± 1.1	5	3.8 ± 0.6	1.1 ± 0.8	5	10.8 ± 0.6	3.3 ± 1.4	5	9.8 ± 0.6	3.0 ± 1.3
6	3.3 ± 0.6	1.0 ± 0.8	6	41.5 ± 0.6	12.7 ± 2.7	6	13.8 ± 0.6	4.2 ± 1.6	6	2.5 ± 0.6	0.8 ± 0.7
7	6.0 ± 0.6	1.8 ± 1.0	7	3.8 ± 0.6	1.2 ± 0.8	7	13.7 ± 0.6	4.2 ± 1.5	7	11.7 ± 0.6	3.6 ± 1.4
8	18.4 ± 0.6	5.6 ± 1.8	8	5.4 ± 0.6	1.6 ± 1.0	8	14.9 ± 0.6	4.6 ± 1.6	8	40.4 ± 0.6	12.3 ± 2.6
9	2.3 ± 0.6	0.7 ± 0.7	9	15.2 ± 0.6	4.6 ± 1.6	9	17.2 ± 0.6	5.3 ± 1.7	9	2.2 ± 0.6	0.7 ± 0.6
10	4.9 ± 0.6	1.5 ± 0.9	10	16.0 ± 0.6	4.9 ± 1.7	10	21.4 ± 0.6	6.5 ± 1.9	10	1.0 ± 0.6	0.3 ± 0.5
11	4.1 ± 0.6	1.2 ± 0.9	11	1.5 ± 0.6	0.5 ± 0.5	11	19.7 ± 0.6	6.0 ± 1.8	11	5.8 ± 0.6	1.8 ± 1.0
12	5.6 ± 0.6	1.7 ± 1.0	12	0.8 ± 0.6	0.2 ± 0.4	12	22.3 ± 0.6	6.8 ± 2.0	12	10.6 ± 0.6	3.2 ± 1.4
13	11.8 ± 0.6	3.6 ± 1.4	13	5.3 ± 0.6	1.6 ± 1.0	13	1.6 ± 0.6	0.5 ± 0.6	13	7.4 ± 0.6	2.3 ± 1.1
14	2.0 ± 0.6	0.6 ± 0.6	14	1.1 ± 0.6	0.3 ± 0.5	14	10.9 ± 0.6	3.3 ± 1.4	14	5.1 ± 0.6	1.6 ± 1.0
15	3.2 ± 0.6	1.0 ± 0.8	15	19.5 ± 0.6	5.9 ± 1.8	15	2.6 ± 0.6	0.8 ± 0.7	15	11.5 ± 0.6	3.5 ± 1.4
16	5.5 ± 0.6	1.7 ± 1.0	16	13.8 ± 0.6	4.2 ± 1.6	16	0.8 ± 0.6	0.2 ± 0.4	16	6.9 ± 0.6	2.1 ± 1.1
17	38.5 ± 0.6	11.8 ± 2.6	17	3.2 ± 0.6	1.0 ± 0.8	17	11.2 ± 0.6	3.4 ± 1.4	17	3.3 ± 0.6	1.0 ± 0.8
18	13.0 ± 0.6	4.0 ± 1.5	18	2.7 ± 0.6	0.8 ± 0.7	18	11.8 ± 0.6	3.6 ± 1.4	18	32.5 ± 0.6	9.9 ± 2.4
19	26.1 ± 0.6	8.0 ± 2.1	19	7.1 ± 0.6	2.2 ± 1.1	19	7.5 ± 0.6	2.3 ± 1.1	19	28.1 ± 0.6	8.6 ± 2.2
20**	171.9 ± 16.5	107.4 ± 12.0	20	5.3 ± 0.6	1.6 ± 1.0	20	8.8 ± 0.6	2.7 ± 1.2	20	28.1 ± 0.6	8.6 ± 2.2
21	55.4 ± 2.9	16.9 ± 3.2	21	4.1 ± 0.6	1.2 ± 0.9	21	22.4 ± 0.6	6.8 ± 2.0	21	16.0 ± 0.6	4.9 ± 1.7
22	18.5 ± 2.4	5.7 ± 1.9	22	36.5 ± 0.6	11.1 ± 2.5	22	24.5 ± 0.6	7.5 ± 2.1	22	5.2 ± 0.6	1.6 ± 1.0
23	15.9 ± 1.5	4.9 ± 1.7	23	13.6 ± 0.6	4.2 ± 1.5	23	6.1 ± 0.6	1.9 ± 1.0	23	27.4 ± 0.6	8.4 ± 2.2
Sum	461.0	195.8 ± 63.1***	24	19.4 ± 0.6	5.9 ± 1.8	24	1.4 ± 0.6	0.4 ± 0.5	24	19.0 ± 0.6	5.8 ± 1.8
			25	17.6 ± 0.6	5.4 ± 1.7	25	1.7 ± 0.6	0.5 ± 0.6	25	16.3 ± 0.6	5.0 ± 1.7
			26	6.1 ± 0.6	1.9 ± 1.0	26	3.4 ± 0.6	1.0 ± 0.8	26	11.1 ± 0.6	3.4 ± 1.4
			27	3.7 ± 0.6	1.1 ± 0.8	27	15.9 ± 0.6	9.9 ± 1.7	27	23.0 ± 0.6	7.0 ± 2.0
			28	12.8 ± 0.6	3.9 ± 1.5	28	1.2 ± 0.6	0.8 ± 0.5	28	10.3 ± 0.6	3.2 ± 1.3
			29	8.3 ± 0.6	2.5 ± 1.2	29	26.0 ± 0.6	8.0 ± 2.1	29	4.8 ± 0.6	1.5 ± 0.9
			30	17.6 ± 0.6	5.4 ± 1.7	30	11.8 ± 0.6	3.6 ± 1.4	30	1.9 ± 0.6	0.6 ± 0.6
			31**	159.3 ± 5.4	99.5 ± 6.8	31	19.7 ± 0.6	6.0 ± 1.8	31	21.0 ± 0.6	6.4 ± 1.9
			32	57.2 ± 1.8	17.5 ± 3.2	32	8.5 ± 0.6	2.6 ± 1.2	32	14.5 ± 0.6	4.4 ± 1.6
			33	5.1 ± 0.7	1.6 ± 1.0	33	15.5 ± 0.6	4.8 ± 1.6	Sum	412.1	126.0 ± 70.8
			34	13.7 ± 1.5	4.2 ± 1.6	34	2.7 ± 0.6	0.8 ± 0.7			
			35	27.4 ± 3.2	8.4 ± 2.4	35	22.0 ± 0.6	6.7 ± 2.0			
			Sum	603.6	235.4 ± 84.0	36**	45.5 ± 5.5	28.4 ± 4.7			
						37**	87.9 ± 4.8	54.9 ± 5.3			
						38	20.6 ± 3.4	6.3 ± 2.1			
						39	54.8 ± 5.4	16.8 ± 3.5			
						Sum	609.7	234.4 ± 87.0			

Notes: Fault identification (ID) is as in Figure 4.

*Uncertainty of each fault's horizontal displacement is calculated as $\sqrt{\left(v * \sec(90° - \alpha)^2 * \Delta\alpha\right)^2 + \left(\tan(90° - \alpha) * \Delta v\right)^2}$. v is the vertical offset and Δv its uncertainty, α is fault dip angle, and $\Delta\alpha$ is its uncertainty.

**Fish Slough fault, calculated with dip angle of 58 ± 9°. Horizontal displacement of all other faults is calculated with dip angle of 73 ± 9°.

***Uncertainty of total horizontal displacement is calculated as

$$\sqrt{\left((v_1 + v_2 + v_3 + \ldots) * \sec(90° - \alpha)^2 * \Delta\alpha\right)^2 + \left(\tan(90° - \alpha) * \Delta v_1\right)^2 + \left(\tan(90 - \alpha) * \Delta v_2\right)^2 + \left(\tan(90 - \alpha) * \Delta v_3\right)^2 +}$$

where v_{ID} is the vertical offset of the respective fault with Δv_{ID} as the uncertainty.

REFERENCES CITED

Allmendinger, R.W., Fisher, D.M., and Cardozo, N., 2012, Structural Geology Algorithms: Vectors and Tensors: Cambridge, UK, Cambridge University Press, 289 p.

Andersen, N.L., Jicha, B.R., Singer, B.S., and Hildreth, W., 2017, Incremental heating of Bishop tuff sanidine reveals preeruptive radiogenic Ar and rapid remobilization from cold storage: Proceedings of the National Academy of Sciences of the United States of America, v. 114, no. 47, p. 12,407–12,412, https://doi.org/10.1073/pnas.1709581114.

Bateman, P.C., Pakiser, L.C., and Kane, M.F., 1965, Geology and tungsten mineralization of the Bishop district, California, with a section on gravity study of Owens Valley and a section on seismic profile: U.S. Geological Survey Professional Paper 470, https://doi.org/10.3133/pp470.

Beanland, S., and Clark, M.M., 1994, The Owens Valley fault zone, Eastern California, and surface faulting associated with the 1872 earthquake: U.S. Geological Survey Bulletin 1982, 29 p.

Berry, M.E., 1997, Geomorphic analysis of Late Quaternary faulting on Hilton Creek, Round Valley and Coyote warp faults, east-central Sierra Nevada, California, USA: Geomorphology, v. 20, no. 1–2, p. 177–195, https://doi.org/10.1016/S0169-555X(97)00033-0.

Blewitt, G., Hammond, W.C., and Kreemer, C., 2018, Harnessing the GPS data explosion for interdisciplinary science: Eos (Transactions, American Geophysical Union), https://doi.org/10.1029/2018EO104623.

Bucknam, R.C., and Anderson, R.E., 1979, Estimation of fault-scarp ages from a scarp-height–slope-angle relationship: Geology, v. 7, no. 1, p. 11–14, https://doi.org/10.1130/0091-7613(1979)7<11:EOFAFA>2.0.CO;2.

Cardozo, N., and Allmendinger, R.W., 2013, Spherical projections with OSXStereonet: Computers & Geosciences, v. 51, p. 193–205, https://doi.org/10.1016/j.cageo.2012.07.021.

Cowgill, E., Gold, R.D., Xuanhua, C., Xiao-Feng, W., Arrowsmith, J.R., and Southon, J., 2009, Low Quaternary slip rate reconciles geodetic and geologic rates along the Altyn Tagh fault, northwestern Tibet: Geology, v. 37, no. 7, p. 647–650, https://doi.org/10.1130/G25623A.1.

Cowie, P.A., Roberts, G.P., Bull, J.M., and Visini, F., 2012, Relationships between fault geometry, slip rate variability and earthquake recurrence in extensional settings: Geophysical Journal International, v. 189, no. 1, p. 143–160, https://doi.org/10.1111/j.1365-246X.2012.05378.x.

Dawers, N.H., Anders, M.H., and Scholz, C.H., 1993, Growth of normal faults: Displacement-length scaling: Geology, v. 21, no. 12, p. 1107–1110, https://doi.org/10.1130/0091-7613(1993)021<1107:GONFDL>2.3.CO;2.

DeLano, K., Lee, J., Roper, R., and Calvert, A., 2019, Dextral, normal, and sinistral faulting across the Eastern California shear zone–Mina deflection transition, California-Nevada, USA: Geosphere, v. 15, no. 4, p. 1206–1239, https://doi.org/10.1130/GES01636.1.

dePolo, C.M., Peppin, W.A., and Johnson, P.A., 1993, Contemporary tectonics, seismicity, and potential earthquake sources in the white mountains seismic gap, west-central Nevada and east-central California, USA: Tectonophysics, v. 225, no. 4, p. 271–299, https://doi.org/10.1016/0040-1951(93)90302-Z.

Dixon, T.H., Miller, M., Farina, F., Wang, H., and Johnson, D., 2000, Present-day motion of the Sierra Nevada block and some tectonic implications for the Basin and Range Province, North American Cordillera: Tectonics, v. 19, no. 1, p. 1–24, https://doi.org/10.1029/1998TC001088.

Dokka, R.K., and Travis, C.J., 1990, Role of the Eastern California shear zone in accommodating Pacific-North American Plate motion: Geophysical Research Letters, v. 17, no. 9, p. 1323–1326, https://doi.org/10.1029/GL017i009p01323.

Faure Walker, J.P., Roberts, G.P., Sammonds, P.R., and Cowie, P., 2010, Comparison of earthquake strains over 10^2 and 10^4 year timescales: Insights into variability in the seismic cycle in the central Apennines, Italy: Journal of Geophysical Research: Solid Earth, v. 115, https://doi.org/10.1029/2009JB006462.

Ferrill, D.A., Stamatakos, J.A., and Sims, D., 1999, Normal fault corrugation: Implications for growth and seismicity of active normal faults: Journal of Structural Geology, v. 21, no. 8–9, p. 1027–1038, https://doi.org/10.1016/S0191-8141(99)00017-6.

Ferrill, D.A., Morris, A.P., McGinnis, R.N., Smart, K.J., Watson-Morris, M.J., and Wigginton, S.S., 2016, Observations on normal-fault scarp morphology and fault system evolution of the Bishop tuff in the Volcanic Tableland, Owens Valley, California, U.S.A: Lithosphere, v. 8, no. 3, p. 238–253, https://doi.org/10.1130/L476.1.

Fossen, H., 2020, Structural Geology: Cambridge, UK, Cambridge University Press, 524 p.

Fossen, H., and Rørnes, A., 1996, Properties of fault populations in the Gullfaks Field, northern North Sea: Journal of Structural Geology, v. 18, no. 2–3, p. 179–190, https://doi.org/10.1016/S0191-8141(96)80043-5.

Friedrich, A.M., Wernicke, B.P., Niemi, N.A., Bennett, R.A., and Davis, J.L., 2003, Comparison of geodetic and geologic data from the Wasatch region, Utah, and implications for the spectral character of Earth deformation at periods of 10 to 10 million years: Journal of Geophysical Research: Solid Earth, v. 108, https://doi.org/10.1029/2001JB000682.

Ganev, P.N., Dolan, J.F., Frankel, K.L., and Finkel, R.C., 2010, Rates of extension along the Fish Lake Valley fault and transtensional deformation in the Eastern California shear zone–Walker Lane belt: Lithosphere, v. 2, no. 1, p. 33–49, https://doi.org/10.1130/L51.1.

Gauthier, B.D.M., and Lake, S.D., 1993, Probabilistic modeling of faults below the limit of seismic resolution in Pelican Field, North Sea, offshore United Kingdom: AAPG Bulletin, v. 77, p. 761–777, https://doi.org/10.1306/BDFF8D4E-1718-11D7-8645000102C1865D.

Goethals, M.M., Niedermann, S., Hetzel, R., and Fenton, C.R., 2009, Determining the impact of faulting on the rate of erosion in a low-relief landscape: A case study using in situ produced ^{21}Ne on active normal faults in the Bishop tuff, California: Geomorphology, v. 103, no. 3, p. 401–413, https://doi.org/10.1016/j.geomorph.2008.07.008.

Guest, B., Niemi, N., and Wernicke, B., 2007, Stateline fault system: A new component of the Miocene–Quaternary Eastern California shear zone: Geological Society of America Bulletin, v. 119, no. 11–12, p. 1337–1347, https://doi.org/10.1130/0016-7606(2007)119[1337:SFSANC]2.0.CO;2.

Hampel, A., and Hetzel, R., 2015, Horizontal surface velocity and strain patterns near thrust and normal faults during the earthquake cycle: The importance of viscoelastic relaxation in the lower crust and implications for interpreting geodetic data: Tectonics, v. 34, no. 4, p. 731–752, https://doi.org/10.1002/2014TC003605.

Hauksson, E., 2000, Crustal structure and seismicity distribution adjacent to the Pacific and North America plate boundary in southern California: Journal of Geophysical Research: Solid Earth, v. 105, p. 13,875–13,903, https://doi.org/10.1029/2000JB900016.

Hetland, E.A., and Hager, B.H., 2005, Postseismic and interseismic displacements near a strike-slip fault: A two-dimensional theory for general linear viscoelastic rheologies: Journal of Geophysical Research: Solid Earth, v. 110, B10401, https://doi.org/10.1029/2005JB003689.

Hetzel, R., Hampel, A., Gebbeken, P., Xu, Q., and Gold, R.D., 2019, A constant slip rate for the western Qilian Shan frontal thrust during the last 200 ka consistent with GPS-derived and geological shortening rates: Earth and Planetary Science Letters, v. 509, p. 100–113, https://doi.org/10.1016/j.epsl.2018.12.032.

Horton, J.D., 2017, The State Geologic Map Compilation (SGMC) geodatabase of the conterminous United States: U.S. Geological Survey Data Release (ver. 1.1, August 2017), https://doi.org/10.5066/F7WH2N65 (accessed 20 July 2023).

Hough, S.E., and Hutton, K., 2008, Revisiting the 1872 Owens Valley, California, Earthquake: Bulletin of the Seismological Society of America, v. 98, no. 2, p. 931–949, https://doi.org/10.1785/0120070186.

Iezzi, F., Roberts, G., Faure Walker, J., Papanikolaou, I., Ganas, A., Deligiannakis, G., Beck, J., Wolfers, S., and Gheorghiu, D., 2021, Temporal and spatial earthquake clustering revealed through comparison of millennial strain-rates from ^{36}Cl cosmogenic exposure dating and decadal GPS strain-rate: Scientific Reports, v. 11, no. 1, 23320, https://doi.org/10.1038/s41598-021-02131-3.

Karakhanyan, A., Vernant, P., Doerflinger, E., Avagyan, A., Philip, H., Aslanyan, R., Champollion, C., Arakelyan, S., Collard, P., Baghdasaryan, H., Peyret, M., Davtyan, V., Calais, E., and Masson, F., 2013, GPS constraints on continental deformation in the Armenian region and Lesser Caucasus: Tectonophysics, v. 592, p. 39–45, https://doi.org/10.1016/j.tecto.2013.02.002.

Kirby, E., Burbank, D.W., Reheis, M., and Phillips, F., 2006, Temporal variations in slip rate of the White Mountain fault zone, Eastern California: Earth and Planetary Science Letters, v. 248, no. 1–2, p. 168–185, https://doi.org/10.1016/j.epsl.2006.05.026.

Kirby, E., Anandakrishnan, S., Phillips, F., and Marrero, S., 2008, Late Pleistocene slip rate along the Owens Valley fault, Eastern California: Geophysical Research Letters, v. 35, no. 1, https://doi.org/10.1029/2007GL031970.

Kreemer, C., and Young, Z.M., 2022, Crustal strain rates in the Western United States and their relationship with earthquake rates: Seismological Research Letters, v. 93, no. 6, p. 2990–3008, https://doi.org/10.1785/0220220153.

Kreemer, C., Chamotrooke, N., and Lepichon, X., 2004, Constraints on the evolution and vertical coherency of deformation in the Northern Aegean from a comparison of geodetic, geologic and seismologic data: Earth and Planetary Science Letters, v. 225, no. 3–4, p. 329–346, https://doi.org/10.1016/j.epsl.2004.06.018.

Le, K., Lee, J., Owen, L.A., and Finkel, R., 2007, Late Quaternary slip rates along the Sierra Nevada frontal fault zone, California: Slip partitioning across the western margin of the Eastern California shear zone–Basin and Range Province: Geological Society of America Bulletin, v. 119, no. 1–2, p. 240–256, https://doi.org/10.1130/B25960.1.

Lee, J., Spencer, J., and Owen, L., 2001, Holocene slip rates along the Owens Valley fault, California: Implications for the recent evolution of the Eastern California shear zone: Geology, v. 29, no. 9, p. 819–822, https://doi.org/10.1130/0091-7613(2001)029<0819:HSRATO>2.0.CO;2.

Lee, J., Stockli, D.F., Owen, L.A., Finkel, R.C., and Kislitsyn, R., 2009, Exhumation of the Inyo Mountains, California: Implications for the timing of extension along the western boundary of the Basin and Range Province and distribution of dextral fault slip rates across the Eastern California shear zone: Tectonics, v. 28, no. 1, https://doi.org/10.1029/2008TC002295.

Lienkaemper, J.J., Pezzopane, S.K., Clark, M.M., and Rymer, M.J., 1987, Fault fractures formed in association with the 1986 Chalfant Valley, California, earthquake sequence: Preliminary report: Bulletin of the Seismological Society of America, v. 77, no. 1, p. 297–305, https://doi.org/10.1785/BSSA0770010297.

Lifton, Z.M., Newman, A.V., Frankel, K.L., Johnson, C.W., and Dixon, T.H., 2013, Insights into distributed plate rates across the Walker Lane from GPS geodesy: Geophysical Research Letters, v. 40, no. 17, p. 4620–4624, https://doi.org/10.1002/grl.50804.

Lifton, Z.M., Lee, J., Frankel, K.L., Newman, A.V., and Schroeder, J.M., 2021, Quaternary slip rates on the White Mountains fault zone, Eastern California: Implications for comparing geologic to geodetic slip rates across the Walker Lane: Geological Society of America Bulletin, v. 133, no. 1–2, p. 307–324, https://doi.org/10.1130/B35332.1.

Lueddecke, S.B., Pinter, N., and Gans, P., 1998, Plio-Pleistocene ash falls, sedimentation, and range-front faulting along the White-Inyo Mountains Front, California: The Journal of Geology, v. 106, no. 4, p. 511–522, https://doi.org/10.1086/516038.

Marrett, R., and Allmendinger, R.W., 1992, Amount of extension on "small" faults: An example from the Viking graben: Geology, v. 20, no. 1, p. 47–50, https://doi.org/10.1130/0091-7613(1992)020<0047:AOEOSF>2.3.CO;2.

Martín-Banda, R., Insua-Arévalo, J.M., and García-Mayordomo, J., 2021, Slip rate variation during the last ~210 ka on a slow fault in a transpressive regime: The Carrascoy fault (Eastern Betic shear zone, SE Spain): Frontiers of Earth Science, v. 8, https://doi.org/10.3389/feart.2020.599608.

Mazzotti, S., Leonard, L.J., Cassidy, J.F., Rogers, G.C., and Halchuk, S., 2011, Seismic hazard in western Canada from GPS strain rates versus earthquake catalog: Journal of Geophysical Research: Solid Earth, v. 116, https://doi.org/10.1029/2011JB008213.

McGinnis, R.N., Morris, A.P., Ferrill, D.A., and Dinwiddie, C.L., 2009, Deformation analysis of tuffaceous sediments in the Volcanic Tableland near Bishop, California: Lithosphere, v. 1, no. 5, p. 291–304, https://doi.org/10.1130/L43.1.

Meade, B.J., Klinger, Y., and Hetland, E.A., 2013, Inference of multiple earthquake-cycle relaxation timescales from irregular geodetic sampling of interseismic deformation: Bulletin of the Seismological Society of America, v. 103, no. 5, p. 2824–2835, https://doi.org/10.1785/0120130006.

Mechernich, S., Schneiderwind, S., Mason, J., Papanikolaou, I.D., Deligiannakis, G., Pallikarakis, A., Binnie, S.A., Dunai, T.J., and Reicherter, K., 2018, The seismic history of the Pisia fault (Eastern Corinth Rift, Greece) from fault plane weathering features and cosmogenic ^{36}Cl dating: Journal of Geophysical Research: Solid Earth, v. 123, no. 5, p. 4266–4284, https://doi.org/10.1029/2017JB014600.

Miller, M.M., Johnson, D.J., Dixon, T.H., and Dokka, R.K., 2001, Refined kinematics of the Eastern California shear zone from GPS observations, 1993–1998: Journal of Geophysical Research: Solid Earth, v. 106, p. 2245–2263, https://doi.org/10.1029/2000JB900328.

Mouslopoulou, V., Walsh, J.J., and Nicol, A., 2009, Fault displacement rates on a range of timescales: Earth and Planetary Science Letters, v. 278, no. 3–4, p. 186–197, https://doi.org/10.1016/j.epsl.2008.11.031.

National Center for Airborne Laser Mapping, 2016, Volcanic Tablelands in Bishop, California: OpenTopography High-Resolution Topography Data and Tools: https://doi.org/10.5069/G9RJ4GCH (accessed December 2022).

Nicol, A., and Wallace, L.M., 2007, Temporal stability of deformation rates: Comparison of geological and geodetic observations, Hikurangi subduction margin, New Zealand: Earth and Planetary Science Letters, v. 258, v. 3–4, p. 397–413, https://doi.org/10.1016/j.epsl.2007.03.039.

Nicol, A., Walsh, J., Mouslopoulou, V., and Villamor, P., 2009, Earthquake histories and Holocene acceleration of fault displacement rates: Geology, v. 37, no. 10, p. 911–914, https://doi.org/10.1130/G25765A.1.

Oskin, M., Perg, L., Blumentritt, D., Mukhopadhyay, S., and Iriondo, A., 2007, Slip rate of the Calico fault: Implications for geologic versus geodetic rate discrepancy in the Eastern California shear zone: Journal of Geophysical Research: Solid Earth, v. 112, https://doi.org/10.1029/2006JB004451.

Oskin, M., Perg, L., Shelef, E., Strane, M., Gurney, E., Singer, B., and Zhang, X., 2008, Elevated shear zone loading rate during an earthquake cluster in Eastern California: Geology, v. 36, no. 6, p. 507–510, https://doi.org/10.1130/G24814A.1.

Papanikolaou, I.D., Roberts, G.P., and Michetti, A.M., 2005, Fault scarps and deformation rates in Lazio–Abruzzo, Central Italy: Comparison between geological fault slip-rate and GPS data: Tectonophysics, v. 408, no. 1–4, p. 147–176, https://doi.org/10.1016/j.tecto.2005.05.043.

Pérouse, E., and Wernicke, B.P., 2017, Spatiotemporal evolution of fault slip rates in deforming continents: The case of the Great Basin region, northern Basin and Range Province: Geosphere, v. 13, no. 1, p. 112–135, https://doi.org/10.1130/GES01295.1.

Phillips, F.M., and Majkowski, L., 2011, The role of low-angle normal faulting in active tectonics of the northern Owens Valley, California: Lithosphere, v. 3, no. 1, p. 22–36, https://doi.org/10.1130/L73.1.

Pinter, N., 1995, Faulting on the Volcanic Tableland, Owens Valley, California: The Journal of Geology, v. 103, no. 1, p. 73–83, https://doi.org/10.1086/629723.

Reheis, M.C., and Dixon, T.H., 1996, Kinematics of the Eastern California shear zone: Evidence for slip transfer from Owens and Saline Valley fault zones to Fish Lake Valley fault zone: Geology, v. 24, no. 4, p. 339–342, https://doi.org/10.1130/0091-7613(1996)024<0339:KOTECS>2.3.CO;2.

Reilinger, R., 1986, Evidence for postseismic viscoelastic relaxation following the 1959 M = 7.5 Hebgen Lake, Montana, Earthquake: Journal of Geophysical Research: Solid Earth, v. 91, no. B9, p. 9488–9494, https://doi.org/10.1029/JB091iB09p09488.

Salditch, L., Stein, S., Neely, J., Spencer, B.D., Brooks, E.M., Agnon, A., and Liu, M., 2020, Earthquake supercycles and Long-Term Fault Memory: Tectonophysics, v. 774, https://doi.org/10.1016/j.tecto.2019.228289.

Salomon, E., Schmidt, S., Hetzel, R., Mingorance, F., and Hampel, A., 2013, Repeated folding during late Holocene earthquakes on the La Cal Thrust fault near Mendoza City (Argentina): Bulletin of the Seismological Society of America, v. 103, no. 2A, p. 936–949, https://doi.org/10.1785/0120110335.

Sarna-Wojcicki, A.M., Pringle, M.S., and Wijbrans, J., 2000, New ^{40}Ar/^{39}Ar age of the Bishop tuff from multiple sites and sediment rate calibration for the Matuyama-Brunhes boundary: Journal of Geophysical Research: Solid Earth, v. 105, no. B9, p. 21,431–21,443, https://doi.org/10.1029/2000JB900901.

Sheridan, M.F., 1970, Fuarmolic mounds and ridges of the Bishop tuff, California: Geological Society of America Bulletin, v. 81, no. 3, p. 851–868, https://doi.org/10.1130/0016-7606(1970)81[851:FMAROT]2.0.CO;2.

Sieh, K., Natawidjaja, D.H., Meltzner, A.J., Shen, C.-C., Cheng, H., Li, K.-S., Suwargadi, B.W., Galetzka, J., Philibosian, B., and Edwards, R.L., 2008, Earthquake supercycles inferred from sea-level changes recorded in the corals of West Sumatra: Science, v. 322, no. 5908, p. 1674–1678, https://doi.org/10.1126/science.1163589.

Stevens, C., Stone, P., and Blakely, R., 2013, Structural evolution of the East Sierra Valley System (Owens Valley and vicinity), California: A geologic and geophysical synthesis: Geosciences, v. 3, no. 2, p. 176–215, https://doi.org/10.3390/geosciences3020176.

Stockli, D.F., Dumitru, T.A., McWilliams, M.O., and Farley, K.A., 2003, Cenozoic tectonic evolution of the White Mountains, California and Nevada: Geological Society of America Bulletin, v. 115, no. 7, p. 788–816, https://doi.org/10.1130/0016-7606(2003)115<0788:CTEOTW>2.0.CO;2.

Thatcher, W., 1983, Nonlinear strain buildup and the earthquake cycle on the San Andreas Fault: Journal of Geophysical Research: Solid Earth, v. 88, no. B7, p. 5893–5902, https://doi.org/10.1029/JB088iB07p05893.

Unruh, J., Humphrey, J., and Barron, A., 2003, Transtensional model for the Sierra Nevada frontal fault system, Eastern California: Geology, v. 31, no. 4, p. 327–330, https://doi.org/10.1130/0091-7613(2003)031<0327:TMFTSN>2.0.CO;2.

Wallace, R.E., 1987, Grouping and migration of surface faulting and variations in slip rates on faults in the Great Basin province: Bulletin of the Seismological Society of America, v. 77, no. 3, p. 868–876, https://doi.org/10.1785/BSSA0770030868.

Walsh, J., Watterson, J., and Yielding, G., 1991, The importance of small-scale faulting in regional extension: Nature, v. 351, no. 6325, p. 391–393, https://doi.org/10.1038/351391a0.

Xu, Q., Hetzel, R., Hampel, A., and Wolff, R., 2021, Slip rate of the Danghe Nan Shan thrust fault from ^{10}Be exposure dating of folded river terraces: Implications for the strain distribution in Northern Tibet: Tectonics, v. 40, no. 4, https://doi.org/10.1029/2020TC006584.